Spin-preserving chiral mirror based on a pattern of rotated elliptical holes in thin monolithic all-dielectric photonic crystal slabs

Qilin Duan,[1] Yali Zeng,[2] Yuhang Yin ⓘ,[3] Shan Zhu,[3] Jinying Xu,[4] Huanyang Chen,[1,*] and Yineng Liu ⓘ[1,†]

[1]*Institute of Electromagnetics and Acoustics, College of Physical Science and Technology,*
Department of Physics, Xiamen University, Xiamen 361005, China
[2]*Key Laboratory of Light Field Manipulation and Information Acquisition Ministry of Industry and Information Technology*
and School of Physical Science and Technology, Northwestern Polytechnical University, Xi'an 710129, China
[3]*Quantum Science Center of Guangdong-Hongkong-Macao Greater Bay Area, Shenzhen 518000, China*
[4]*Department of Physics, Fuzhou University, Fuzhou 350108, China*

Spin-preserving chiral mirrors, which reflect only one spin state of light under normal illumination without reversing the light's handedness, are intrinsically chiral structures. These mirrors are of particular interest for applications in optical imaging, chiral quantum optics, chiral cavities, and the recognition and sensing of chiral molecules. However, most of them are limited by complicated chiral elements of their unit cells and multilayer structures, which are challenging to fabricate and integrate in the visible-near-infrared region. Here we propose a thin monolithic photonic crystal (PhC) mirror with elliptical air holes to realize a giant intrinsic chiroptical response. Beyond the past chiral mirrors, our chiral mirrors selectively reflect only one spin state of light while preserving its handedness, exhibiting a near unity of circular dichroism (CD). The working principle of the PhC chiral mirror is based on guided-mode resonance with the simultaneous excitation of transverse electric (TE) and transverse magnetic (TM) eigenmodes. Interestingly, the TE and TM bands can be dynamically adjusted via the orientation angle of the elliptical air holes, leading to their degeneracy at a certain orientation angle. Based on the modified coupled mode theory, we show that the key point to achieving giant intrinsic CD is the angular difference in the in-plane effective orientation of the TE and TM eigenmode currents. As a proof of concept, we designed such an easy-fabrication PhC to serve as a spin-preserving chiral mirror, which shows superiority to the previously reported structure. The results of this work may provide new possibilities for compact chiral sensing, imaging, and polarization-sensitive devices.

I. INTRODUCTION

Unlike traditional mirrors, spin-preserving chiral mirrors [1,2] that selectively reflect only one spin state of light while preserving its helicity are chiroptical structures of widespread applications in chiral imaging [3], chiral quantum optics [4], chiral cavities [5], and chiral molecule recognition and sensing [6]. More recently, some methods to obtain the intrinsically chiral mirror have been proposed in both theory and experiment through chiral metamaterials and quasi-2D metasurfaces. However, the realization of a thin monolithic chiral mirror still has some challenges. First, the intrinsic chirality under normal incidence requires the simultaneous excitation of in-plane magnetic and electric dipoles, which is the main challenge to achieving a spin-preserving chiral mirror in monolithic planar all-dielectric structures. Since intrinsic chiroptical effects in the thin 2D lossless structures are usually prohibited due to the difficult excitation of in-plane magnetic dipoles. Recently, metastructures

consisting of 2D subwavelength arrays of three-dimensional chiral elements, such as the typical chiral elements containing spiral shapes [7] and multilayer structures [8], have been proposed to address this issue. However, the fabrication technology and integration of chiral elements at the nanoscale are challenging. Subsequently, some 2D/planar counterparts without breaking the symmetry along the *z*-direction symmetry were proposed to alleviate this challenge. For example, planar ultrathin chiral plasmonic metasurfaces with reduced in-plane symmetry have been designed to manipulate intrinsic chiral response, like nanoslits [9] and fish-scale plasmonic structures [10]. Despite progress, the inevitable ohmic losses still hinder real-life applications. Therefore, the planar all-dielectric chiral metasurface with low loss and high refractive index becomes an ideal platform for intrinsic chirality [11]. When the planar all-dielectric structure possesses a proper thickness, not only in-plane magnetic moments, but even higher-order moments can be effectively excited to achieve intrinsic chirality. By way of illustration, the large intrinsic circular dichroism (CD) in a variety of all-dielectric metasurfaces has been achieved, such as Z-shaped metaatoms [12] and gammadion-shaped metasurfaces [13]. However, these metasurfaces mainly exhibit selective chiral transmission through

---

*Contact author: kenyon@xmu.edu.cn
†Contact author: lyn610@xmu.edu.cn

high-order multipole selective excitation, such as magnetic octupole.

Second, upon normal illumination, the handedness preservation of reflected light is also a challenge. While conventional mirrors or uniform interfaces reflect linear polarizations without polarization change, the helicity of circularly polarized waves is reversed upon reflection. The recently developed "magical mirrors" that reflect one circular polarized light (CPL) without a spin-state change while completely absorbing the other CPL with the opposite handedness have been demonstrated using planar metasurfaces with back metallic mirrors [14–16]. In principle, to achieve perfect absorption of the selected polarization, the back metallic mirrors are indispensable in 2D planar metasurfaces. Although the developed "magical mirrors" have shown great performance, the realization of spin-preserving chiral mirrors in monolithic planar all-dielectric structures with lower loss, lighter weight, and ease of integration remains a challenge.

To overcome the two main challenges mentioned above, a class of geometrically straightforward optical structures to boost their chiroptical performances was presented. Metasurfaces containing rotated rods or air holes are easy to fabricate and possess an additional degree of freedom to manipulate light, such as a rotated angle. This kind of metaatom has been widely used to control the light through the Pancharatnam-Berry geometric phase [17,18]. Then the chiroptical response in such geometrically simple platforms was reported. As well known, elliptical or rectangular structures have anisotropy for x-polarized and y-polarized light [19,20], so by simply rotating the elliptical or rectangular structures [21–27], the chiroptical response can occur. Although these planar all-dielectric structures can lead to exotic chiroptical effects such as circular conversion dichroism and asymmetric transmission, it is crucial to note that they remain fundamentally distinct from the intrinsic chirality characteristic of spin-preserving mirrors. Very recently, Semnani *et al.* have developed a spin-preserving mirror utilizing a PhC, featuring a unique tripartite arrangement of perforated holes [28]. The principle of the PhC mirror is based on guided-mode resonance (GMR), which involves the concurrent stimulation of leaky transverse electric (TE) and transverse magnetic (TM) Bloch modes within the PhC. Despite its excellent intrinsic chirality performance, the structural units are still complex. In fact, this tripartite arrangement of perforated holes can be simply replaced by single elliptical air holes, which both possess C_2 rotational symmetry and mirror symmetry in the z direction. The strong intrinsic chirality can be achieved with these simpler and more intuitive structures, besides, the introduced rotational degree of freedom offers a richer platform for further investigating the underlying mechanisms containing two eigenmodes [29].

Here we propose a thin monolithic PhC slab with elliptical air holes to achieve a spin-preserving mirror by its giant intrinsic chiroptical response. The PhC slab introduces an orientation angle as a tunable degree of freedom for the TE and TM bands. By rotating the elliptical air holes, the degeneracy for the TE and TM eigenmodes is revealed in the visible-near-infrared (NIR) region and leads to a giant chiroptical response (CD = 0.92), which can selectively reflect
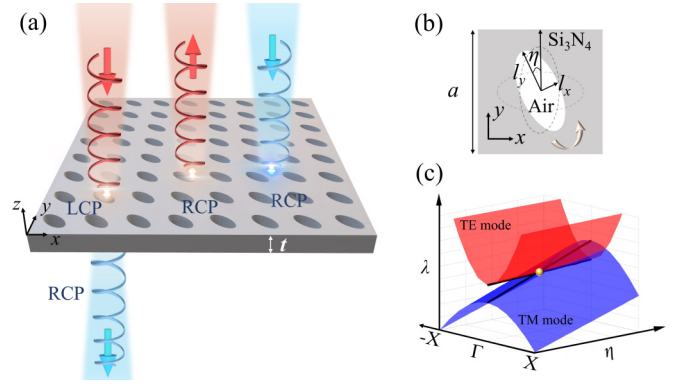

FIG. 1. (a) Schematic of the chiroptical response of the designed PhC at the resonant wavelength. (b) The unit cell of the planar PhC with rotated elliptical air holes. (c) The diagram shows the TE (red surface) and TM eigenmode (blue surface) with the variation of orientation angle η and k vector near Γ point, the black lines denote the at-Γ eigenmode for TE and TM mode tuned by orientation angle, the degeneracy point of TE and TM eigenmode is marked by yellow dot.

the one-handedness of light without reversing its helicity. To get a deeper understanding of this phenomenon, the coupled mode theory (CMT) considering TE and TM eigenmodes is developed. Combining the modified CMT and numerical simulation, we conclude that achieving significant chirality requires the angle difference between the effective currents of the TE and TM modes to be 45 degrees. Moreover, the near-field electromagnetic fields also depict the relationship at TE and TM mode degeneracy point, where the effective currents of the eigenmodes are nearly at a 45-degree angle to each other. To elucidate the underlying physics of the significant chirality, we further illustrate this phenomenon from the perspective of electromagnetic multipole analysis, demonstrating the alignment of the electromagnetic multipoles forms a nearly 45-degree relationship between the effective currents. In the end, we designed such an easy-fabrication PhC to act as a spin-preserving chiral mirror, which has been proven to be superior to the previously reported structure. Our work could provide new possibilities for compact chiral sensing, imaging, and polarization-sensitive devices.

II. STRUCTURE DESIGN AND THE CHIROPTICAL RESPONSE OF THE PLANAR PHOTONIC CRYSTAL

Figure 1(a) shows the schematic diagram of the different responses to LCP and RCP incident light for a PhC slab with rotated elliptical air holes. Under normal illumination, the ideal spin-preserving mirror totally reflects one spin state of light without changing its handedness, while the incident light with opposite handedness is transmitted as shown in Fig. 1(a). Figure 1(b) displays the square unit cell structure from the top view, and its structure parameters are $a = 700$ nm, $l_x = 127$ nm, $l_y = 254$ nm, and $t = 371$ nm. The square unit cell is composed of Si$_3$N$_4$ (refractive index $n = 2.02$) with elliptical air holes, showing C_2 rotation symmetry around the z axis. Here the elliptical air holes can rotate within the $x-y$ plane with an orientation angle η, which will break all the in-plane
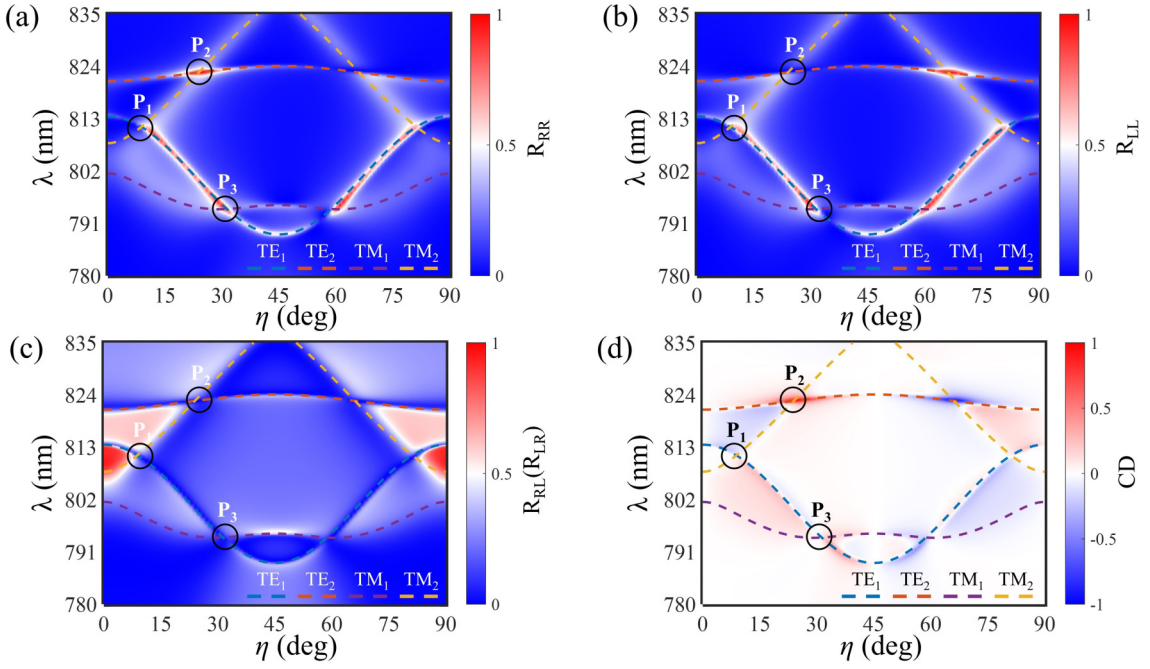
FIG. 2. (a), (b) The copolarization reflection spectra (R_{RR} and R_{LL}, respectively) of the PhC concerning the orientation angle and wavelength. (c) The cross-polarization reflection spectra (R_{RL}/R_{LR}) of the PhC concerning the orientation angle and wavelength. (d) CD spectra of the PhC with the variation of the orientation angle and wavelength at normal incidence. Here the dotted lines are the at-Γ eigen-wavelengths of TE/TM modes, and the three degeneracy points of the TE and TM modes are marked by P_1, P_2, and P_3, respectively.

mirror symmetry of the lattice for $\eta \neq n \times 45°(n \in \mathbb{Z})$. While for $\eta = n \times 45°(n \in \mathbb{Z})$, two in-plane mirror symmetries will be preserved, thus no chiroptical response will appear. Besides, the PhC has mirror symmetry along the z direction, thus the GMR of the PhC can be divided into TE and TM eigenmodes [30,31]. As shown in Fig. 1(c), the eigen-wavelengths of TE and TM modes can be flexibly tuned by orientation angle around Γ point. The two black lines denote the at-Γ TE and TM eigenmode, corresponding to the normal incidence. Clearly, with the variation of orientation angle, the TE and TM modes will degenerate, here the degeneracy point is marked by a yellow sphere. The degeneracy of TE and TM eigenmodes is indispensable for giant intrinsic chiroptical response in PhCs with C_2 symmetry. Based on this principle, We naturally raise such a crucial question: how does the degeneracy of TE and TM eigenmodes lead to intrinsic giant chirality for spin-preserving chiral mirrors?

To explore the chiroptical response concerning orientation angle η and wavelengths in the PhC, the reflection spectra for normal incidence of CPL, and the eigen-wavelengths of TE and TM modes at Γ point corresponding to normal incidence in real space are shown in Fig. 2. The simulation is performed using 3D Finite Element simulation software Comsol Multiphysics. We can use the Jones matrix under a circular basis to describe the reflection of the system. The reflection is $R_{ij} = |r_{ij}|^2$, here r_{ij} is the reflection coefficient in the Jones matrix, and i, j denote the polarization state of the reflected and incident wave, respectively, which can be presented as RCP(R) and LCP(L) wave. The chiroptical response of the system can be expressed by CD = $R_{RR} + R_{LR} - R_{LL} - R_{RL}$. It is important to note that, with the wave vector being reversed for the incident and reflected

CPL, the handedness of the reflected CPL is inverted relative to that of the incident CPL when the observation plane remains constant.

To see the chiroptical response of the chiral mirror intuitively, we start by analyzing the reflection acquired from the Jones matrix. As shown in Figs. 2(a) and 2(b), we plot the copolarization reflection R_{RR} and R_{LL} of the Jones matrix, respectively. Besides, to study the influence of the Bloch eigenmode on the chiroptical response, we also plot the eigen-wavelengths of the leaky TE and TM eigenmodes at Γ point in the wavelength range in Figs. 2(a)–2(d), which are marked as TE_1, TE_2, TM_1, and TM_2 modes through different colored dashed lines. The TE and TM bands can be manipulated by the orientation angle η and have three degeneracy points at $\eta = 8.8°$ (P_1 point), $23.9°$ (P_2 point), and $31.3°$ (P_3 point), respectively (the enlarged views of the three degeneracy points are shown in Fig. S3 in the Supplemental Material [32]). The near-unity spin-preserving reflection appears at the orientation angle $\eta = 24.8°$ in Fig. 2(a), while the reflection of the opposite handedness at the same orientation angle in Fig. 2(b) is almost zero. Thus, the PhC fully reflects the RCP incident wave without reversing its helicity at $\eta = 24.8°$, forming a spin-preserving mirror in planar PhC with a simplified and tunable structure. Similarly, the value is reversed for R_{RR} and R_{LL} at $\eta = 65.2°$, which in turn fully reflects the LCP incident wave without reversing its helicity. Since the orientation angle will only break all the in-plane mirror symmetry while still preserving the C_2 symmetry, thus the cross-polarization reflection is the same ($R_{LR} = R_{RL}$) as shown in Fig. 2(c). The R_{LR} (R_{RL}) are nearly zero at the three degeneracy points. We can also notice from Figs. 2(a) and 2(b) that the near-unity reflection only appears near the degeneracy point P_2.

Meanwhile, all the peaks of the R_{RR} and R_{LL} in Figs. 2(a) and 2(b) are along the TE and TM bands, which indicates the excitation of the Bloch eigenmode in the PhC.

Based on these reflection spectra of the Jones matrix, we get the CD value accordingly. The CD spectra with the variation of orientation angle η is shown in Fig. 2(d). We find that the variation of the orientation angle η can tune the value of the CD. Meanwhile, the magnitude of the CD is symmetric with $\eta = 45°$. Still, the sign of CD is reversed, and the two complementary angles that exhibit the same magnitude of CD have the relationship $\eta_1 + \eta_2 = 90°$, which forms chiral enantiomers with opposite CD. The magnitude of CD is small at individual TE and TM bands ($|CD| < 0.5$), and the maximum magnitude of CD = 0.92 appears near the P_2 point at $\eta = 24.8°$, the reason for the slight deviation from the degeneracy point will be illustrated in the next section. However, the CD is nearly zero at P_1 and P_3 points, indicating that the interaction of TE and TM modes cannot always lead to a strong chiroptical response. The reason behind this phenomenon is explored in the next section. Here we only focus on the spin-preserving phenomenon for reflection, the transmission spectra of this monolithic PhC are shown in Fig. S6 in the Supplemental Material [32].

III. CHIROPTICAL RESPONSE OF THE DEGENERACY OF TE AND TM EIGENMODES

To understand the intrinsic chirality in the PhC, we develop the CMT theory to further quantitatively illustrate the reason for the different chiroptical responses at the three degeneracy points in Fig. 2. The CMT for the single TE/TM mode is shown in Sec. 1 in the Supplemental Material [32] (see also Refs. [29,33–35] therein). Here, we propose the modified CMT for the degeneracy of TE and TM modes. The main equation of the dual mode CMT can be written as

$$\frac{d\mathbf{p}}{dt} = (i\mathbf{\Omega} - \mathbf{\Gamma})\mathbf{p} + \mathbf{M}^{\mathrm{T}}\mathbf{a},$$
$$\mathbf{b} = \mathbf{S}\mathbf{a} = \mathbf{M}\mathbf{p} + \mathbf{C}\mathbf{a}, \quad (1)$$

where, $\mathbf{a} = [a_R \quad a_L \quad a'_R \quad a'_L]^{\mathrm{T}}$, $\mathbf{b} = [b_R \quad b_L \quad b'_R \quad b'_L]^{\mathrm{T}}$, $\mathbf{p} = (p_{TE} \quad p_{TM})^{\mathrm{T}}$, $\mathbf{\Omega} = \begin{pmatrix} \omega - \omega_{TE} & 0 \\ 0 & \omega - \omega_{TM} \end{pmatrix}$, $\mathbf{\Gamma} = \begin{pmatrix} \gamma_{TE} & g \\ g & \gamma_{TM} \end{pmatrix}$, $\mathbf{M} = \begin{pmatrix} m_{TER} & m_{TEL} & m'_{TER} & m'_{TEL} \\ m_{TMR} & m_{TML} & m'_{TMR} & m'_{TML} \end{pmatrix}^{\mathrm{T}}$, $\mathbf{a}$ and $\mathbf{b}$ are the normal input and output waves at two ports of the photonic crystal mirror and the subscript L/R means the LCP/RCP polarized light, $\mathbf{p}$ is the complex amplitude of the oscillating eigenmode, $\mathbf{\Omega}$ is the mode's resonant frequency, $\mathbf{\Gamma}$ is the decay rate due to the radiation, $\mathbf{S}$ is the scattering matrix, $\mathbf{M}$ is the coupling matrix between the resonances with incident and outgoing waves, and the subscript TE and TM refer to TE and TM eigenmodes, respectively. The nonresonant background $\mathbf{C}$ has the form

$$\mathbf{C} = \begin{pmatrix} 0 & \rho & \tau & 0 \\ \rho & 0 & 0 & \tau \\ \tau & 0 & 0 & \rho \\ 0 & \tau & \rho & 0 \end{pmatrix}. \quad (2)$$

Due to energy conservation, $\mathbf{C}$ in Eq. (2) needs to satisfy the relationship $\mathbf{C}^\dagger \mathbf{C} = \mathbf{I}$. Thus, two real parameters can be

introduced to express the background scattering coefficients:

$$\tau = e^{i\alpha}\cos\beta, \quad \rho = ie^{i\alpha}\sin\beta, \quad (3)$$

where phase α varies from 0 to 2π, and β varies from $-\pi/2$ to $\pi/2$. Obviously, α affects the phase of reflection, and β is related to the amplitude of reflection. For a dielectric PhC, the background scattering coefficients show no chiroptical response; besides, these coefficients rely on the material and the thickness of the slab [36]. Apart from the background scattering coefficients, the coupling coefficients in matrix $\mathbf{M}$ in Eq. (1) for TE and TM eigenmodes to RCP and LCP wave can be written as (the detailed derivations are shown in Sec. 1 in the Supplemental Material [32], see also Ref. [29] therein):

$$m_{TER} = i\sqrt{\frac{\gamma_{TE}}{2}}e^{i\frac{\alpha+\beta}{2}-i\theta_{TE}}, \quad m_{TEL} = i\sqrt{\frac{\gamma_{TE}}{2}}e^{i\frac{\alpha+\beta}{2}+i\theta_{TE}}, \quad (4)$$

$$m_{TMR} = \sqrt{\frac{\gamma_{TM}}{2}}e^{i\frac{\alpha-\beta}{2}-i\theta_{TM}}, \quad m_{TML} = \sqrt{\frac{\gamma_{TM}}{2}}e^{i\frac{\alpha-\beta}{2}+i\theta_{TM}}. \quad (5)$$

Here, the θ_{TE}/θ_{TM} is the effective orientation angle of the eigenstate current within the xy plane. Specifically, this parameter is reliant on the geometrical structure: The orientation angle of the elliptical air holes in the PhC mirror. We can see from Eqs. (4) and (5) that the magnitude of the coupling coefficients of TE/TM eigenmode to LCP and RCP are always the same, thus, the CD is very small at individual TE and TM eigenmodes shown in Fig. S2 in the Supplemental Material [32]. Meanwhile, Eqs. (4) and (5) obey the following relationship due to the even/odd function of current corresponding to the TE or TM eigenmode along the z direction:

$$m'_{TER} = m_{TEL}, m'_{TEL} = m_{TER}, \quad (6)$$

$$m'_{TMR} = -m_{TML}, m'_{TML} = -m_{TMR}. \quad (7)$$

The matrix $\mathbf{M}$ also needs to satisfy the following relationship due to the energy conservation:

$$\mathbf{M}^\dagger \mathbf{M} = 2\mathbf{\Gamma}. \quad (8)$$

Thus, we can get the far-field coupling $g = 0$ in $\mathbf{\Gamma}$ matrix between TE and TM mode by substituting Eqs. (6) and (7) into Eq. (8). Therefore, The $\mathbf{S}$-matrix in Eq. (1) can be derived as

$$\mathbf{S} = \begin{pmatrix} r_{RR} & r_{RL} & t'_{RR} & t'_{RL} \\ r_{LR} & r_{LL} & t'_{LR} & t'_{LL} \\ t_{RR} & t_{RL} & r'_{RR} & r'_{RL} \\ t_{LR} & t_{LL} & r'_{LR} & r'_{LL} \end{pmatrix},$$

$$= \mathbf{C} - \mathbf{M}\left[i\begin{pmatrix} \omega - \omega_{TE} & 0 \\ 0 & \omega - \omega_{TM} \end{pmatrix} - \mathbf{\Gamma}\right]^{-1}\mathbf{M}^{\mathrm{T}}. \quad (9)$$

The detailed expressions of the elements in matrix $\mathbf{S}$ are shown in Sec. 2 in the Supplemental Material [32]. Given that the eigenmodes of the PhC determine the values of $\omega_{TE/TM}$ and $\gamma_{TE/TM}$, we only need to ascertain four unknown parameters α, β, θ_{TE}, and θ_{TM}. According to the matrix $\mathbf{S}$, the CD

can be written as

$$CD = R_{RR} - R_{LL} = |r_{RR}|^2 - |r_{LL}|^2 = -\left\{ \frac{\gamma_{TE}\gamma_{TM}[(\gamma_{TE}\omega_1 - \gamma_{TM}\omega_2)\cos(2\beta) + (\gamma_{TE}\gamma_{TM} + \omega_2\omega_1)\sin(2\beta)]\sin[2(\theta_{TE} - \theta_{TM})]}{(\gamma_{TE}^2 + \omega_2^2)(\gamma_{TM}^2 + \omega_1^2)} \right\},$$

(10)

where $\omega_1 = \omega_{TM} - \omega$ and $\omega_2 = \omega_{TE} - \omega$. The CD can be simplified as the following when the TE and TM modes (GMR) have the same resonant frequency $\omega = \omega_0$, $\omega_{TE} = \omega_0$ and $\omega_{TM} = \omega_0$:

$$CD = -\sin(2\beta)\sin[2(\theta_{TE} - \theta_{TM})].$$

(11)

We can deduce from Eq. (11) that the CD is only related to β and $\theta_{TE} - \theta_{TM}$, which corresponds to the nonchiral background scattering and the angular difference in the effective orientation of the eigenstate currents within the xy-plane for TE and TM eigenmodes. The magnitude of CD will be maximal when $\beta = \pm(45° + n \times 90°)$ and $\theta_{TE} - \theta_{TM} = \pm(45° + n \times 90°)(n \in \mathbb{Z})$. Note that for the more general and complicated expression in Eq. (10), due to the influence of both β and $\theta_{TE} - \theta_{TM}$, the maximal magnitude of CD will have the potential to appear when $\omega_1 \neq 0$ and $\omega_2 \neq 0$. This explains why the wavelength corresponding to the maximum CD will slightly deviate from the degeneracy point of TE and TM modes.

Different from the P_2 and P_3 points in Fig. 2(a) which can only consider the interaction of TE and TM modes, four modes should be considered due to the proximity of the four bands at P_1 points. Similarly, for Eq. (1), here $\mathbf{p} = (p_{TE1} \quad p_{TE2} \quad p_{TM1} \quad p_{TM2})^T$,

$$\boldsymbol{\Omega} = \begin{pmatrix} \omega - \omega_{TE1} & 0 & 0 & 0 \\ 0 & \omega - \omega_{TE2} & 0 & 0 \\ 0 & 0 & \omega - \omega_{TM1} & 0 \\ 0 & 0 & 0 & \omega - \omega_{TM2} \end{pmatrix},$$

$$\boldsymbol{\Gamma} = \begin{pmatrix} \gamma_{TE1} & g_1 & 0 & 0 \\ g_1 & \gamma_{TE2} & 0 & 0 \\ 0 & 0 & \gamma_{TM1} & g_2 \\ 0 & 0 & g_2 & \gamma_{TM2} \end{pmatrix}, \quad \text{and} \quad \mathbf{M} =$$

$$\begin{pmatrix} m_{TE1R} & m_{TE2R} & m_{TM1R} & m_{TM2R} \\ m_{TE1L} & m_{TE2L} & m_{TM1L} & m_{TM2L} \\ m'_{TE1R} & m'_{TE2R} & m'_{TM1R} & m'_{TM2R} \\ m'_{TE1L} & m'_{TE2L} & m'_{TM1L} & m'_{TM2L} \end{pmatrix}.$$ Through substituting the

$\mathbf{M}$ matrix to Eq. (8) and considering Eqs. (6) and (7), we can get the value of g_1 and g_2 corresponding to the far-field coupling of $TE_1 - TE_2$ and $TM_1 - TM_2$ modes as follows:

$$g_1 = \sqrt{\gamma_{TE1}\gamma_{TE2}}\cos(\theta_{TE1} - \theta_{TE2}),$$

(12)

$$g_2 = \sqrt{\gamma_{TM1}\gamma_{TM2}}\cos(\theta_{TM1} - \theta_{TM2}).$$

(13)

The $\mathbf{S}$ matrix can also be acquired through Eq. (9).

Leveraging the modified CMT, we can fit both the reflection and CD spectra, along with the phase of the reflection coefficient at the three degeneracy points. This approach facilitates the identification of four critical unknown parameters (α, β, θ_{TE}, and θ_{TM}), which is helpful for us to reveal the physical mechanisms of chiroptical responses induced by orientation angles. In Figs. 3(d)–3(i), the lines represent the numerical results, while the solid spheres denote the fitting results obtained from CMT. The numerical and theoretical

results fit well for both the reflection and phase spectra in Fig. 3. First, Fig. 3(a) shows the unit cell of $\eta = 8.8°$, corresponding to the degeneracy of TE_1 and TM_2 band of Fig. 2. Since the PhC mirror has mirror symmetry along the z direction, thus $R_{RL} = R_{LR}$, we only plot the $R_{RL} = |r_{RL}|^2$ and the phase of r_{RL}. In Fig. 3(d), we can see the $R_{LL} \cong R_{RR}$ at the degeneracy point, which is indicated by the gray dotted line, leading to $CD = -0.023$ at $\lambda = 811.3$ nm. Besides, the magnitude of CD is lower than 0.2 near the degeneracy point, showing a weak chiroptical response caused by the interaction of TE_1 and TM_2 bands. The phase diagram in Fig. 3(g) shows the resonance at the P_1 point. The four fitting parameters are shown in Table 1, from which we can see that $\theta_{TE1} \cong \theta_{TM2}$, resulting in $\sin[2(\theta_{TE} - \theta_{TM})] \cong 0$. This is the reason for the near-zero CD at the P_1 point. Note that in this case, the CD is mainly affected by θ_{TE1} and θ_{TM2} compared with θ_{TE2} and θ_{TM1} as shown in Fig. S7 in the Supplemental Material [32].

For the structure with $\eta = 24.8°$ in Fig. 3(b), the CD is 0.92 at $\lambda = 822.9$ nm as shown in Fig. 3(e). We can only consider TE_2 and TM_2 eigenmodes during the fitting process. The fitting results lead to $\sin[2(\theta_{TE} - \theta_{TM})] \cong 0.97$. Besides, β is larger than that for $\eta = 8.8°$, these two factors both contribute to the giant chirality. The phase spectra also fit well between the numerical results and CMT as shown in Fig. 3(h). The structure of the third degeneracy point for $\eta = 31.3°$ is shown in Fig. 3(c). Similar to the P_1 point, the interaction of TE_1 and TM_1 eigenmodes leads to a weak chiroptical response as shown in Fig. 3(f). The reason can also be found in the fitting results in Table 1, the nearly orthogonal θ_{TE1} and θ_{TM1} lead to $\sin[2(\theta_{TE} - \theta_{TM})] \cong 0$. In Fig. 3(i), the spectral lines of the phase are in excellent agreement with the CMT. These results prove the accuracy of the modified CMT in analyzing the chiroptical response of the planar PhC with rotated elliptical air holes.

In addition, the achiral background coefficients (α and β) in Table 1 strongly depend on the thickness and the effective index of the PhC rather than the specific structure of the PhC [36]. Therefore, the thickness of the PhC has the most significant impact on the CD, while the long and short axes of the elliptical air holes have a slight effect as shown in Fig. S5 in the Supplemental Material [32]. Besides thickness, the orientation angle acts as a crucial parameter manipulating the chiroptical response, as they result in varied effective current orientations of the TE and TM eigenmodes. Thus, it is very important to find a straightforward way to define the effective current orientations (θ_{TE} and θ_{TM} in CMT) with the variation of orientation angle η.

Due to the leakage radiation of TE and TM modes in GMR to the far field, it can be inferred that the far-field radiation will exhibit characteristics of near-field current distribution.
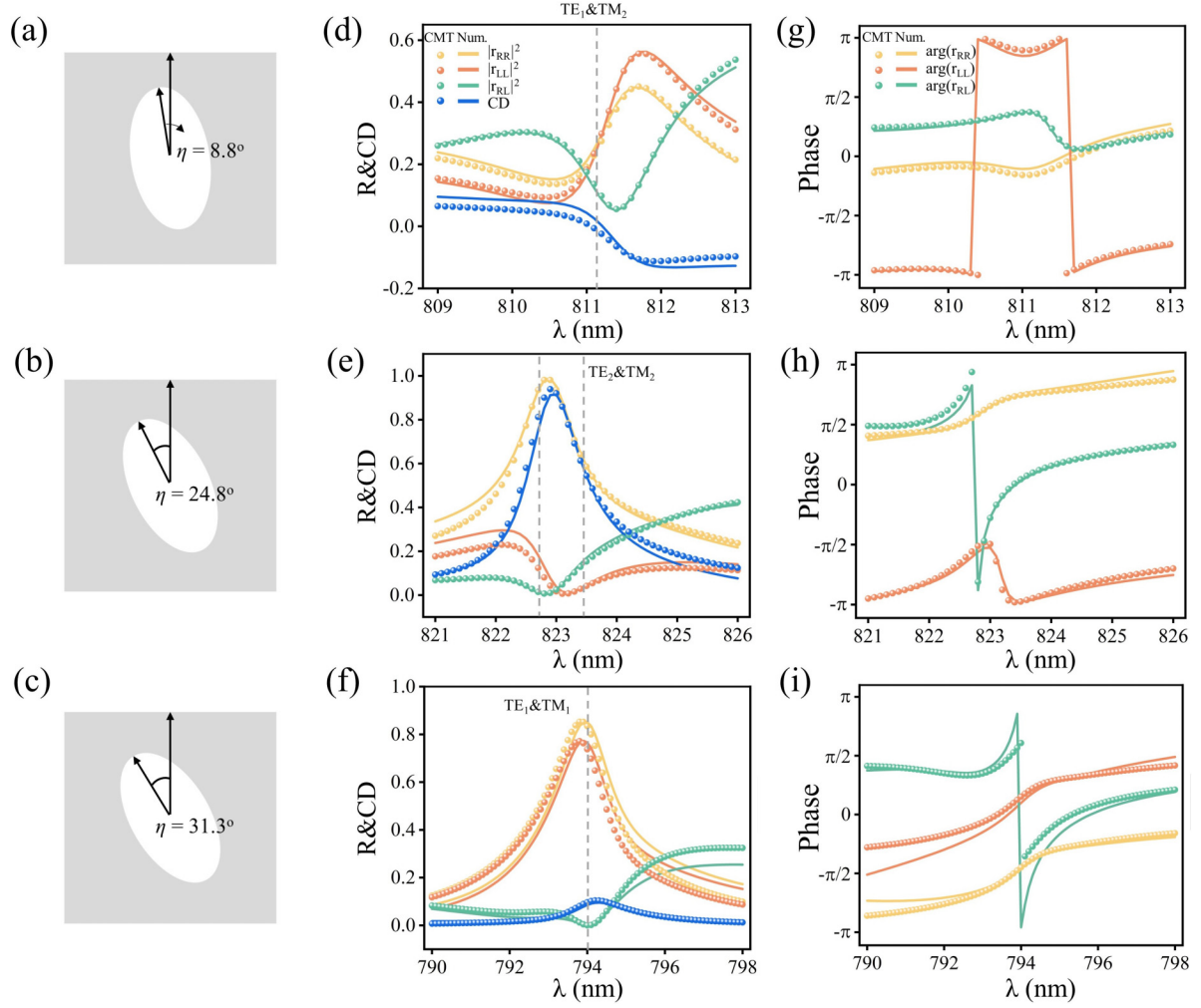
FIG. 3. (a)–(c) Schematic diagrams of the PhC for different orientation angles $\eta = 8.8°$, $24.8°$, and $31.3°$, respectively, which correspond to the P$_1$, P$_2$, and P$_3$ points in Fig. 2(a). (d)–(f) Simulated and fitted reflection and CD spectra for $\eta = 8.8°$, $24.8°$, and $31.3°$, respectively. (g)–(i) Simulated and fitted phase spectra of different elements of the Jones matrix for $\eta = 8.8°$, $24.8°$, and $31.3°$, respectively.

In Fig. 4(a), we show the azimuthal angles ψ of the far-field eigen-polarization states of TE$_1$/TE$_2$ and TM$_1$/TM$_2$ modes in Fig. 2(a) with the variation of orientation angles η. The ψ is defined as $\frac{\arg(S_1 + iS_2)}{2}$, here S_1 and S_2 are Stokes parameters [37]. The trend of the variation of ψ with η is different for each TE$_1$/TE$_2$ and TM$_1$/TM$_2$ band. The corresponding fitting angle results are in Table 1 for the three degeneracy angles are marked with squares in Fig. 4(a). The fitting results agree well with the numerical far-field eigen-polarization eigenstates, which means the effective current orientation (θ_{TE} and θ_{TM}) in the CMT can be acquired simply from azimuthal angles ψ of the far-field polarization, and their relationship can be expressed as $\theta_{TE}(\eta) \cong \psi_{TE}(\eta)$, $\theta_{TM}(\eta) \cong \psi_{TM}(\eta)$. Thus,

Eq. (11) can be written as

$$\text{CD} = -\sin(2\beta)\sin\{2[\psi_{TE}(\eta) - \psi_{TM}(\eta)]\}. \quad (14)$$

As shown in Fig. 4(a), for the orientation angles η that preserve in-plane mirror symmetry, i.e., when $\eta = 0°$ and $90°$, the absolute value of ψ_{TE} and ψ_{TM} will be either $0°$ or $90°$. When $\eta = 45°$, the absolute value of ψ_{TE} and ψ_{TM} will be $45°$, thus leading to $\sin\{2[\psi_{TE}(\eta) - \psi_{TM}(\eta)]\} = 0$, no chiroptical response will appear at these orientation angles of elliptical air holes. Then, we can substitute the azimuthal angles $\psi(\eta)$ to the CMT, since we mainly focus on the $\theta(\eta)$, here, we chose $\beta = 0.5$ as a constant, which is within the range of the fitted value for β as shown in Table 1. The CD spectra

TABLE I. The fitting results of the reflection and CD spectra for $\eta = 8.8°$, $24.8°$, and $31.3°$, respectively.

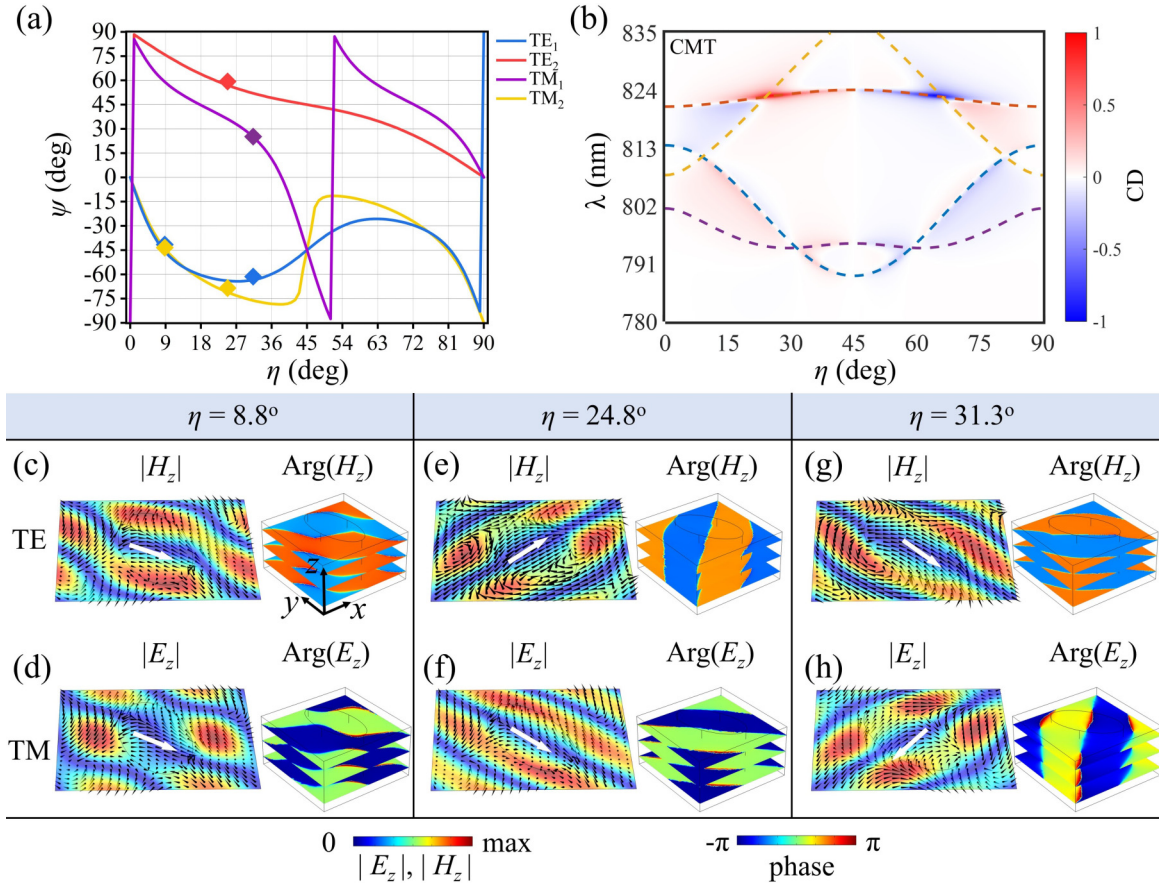| η(deg)	α	β	θ_{TE1}(deg)	θ_{TE2}(deg)	θ_{TM1}(deg)	θ_{TM2}(deg)
8.8	0.0020	0.4610	−41.5910	80.2542	64.2687	−43.4875
24.8	0.2500	0.5730	—	59.2954	—	−68.4799
31.3	−0.4230	0.4901	−61.4211	—	25.1758	—

FIG. 4. (a) The azimuthal angles of the at-Γ eigen-polarization states of TE/TM modes with the variation of orientation angles. The squares in the figure are the fitted results of the current orientations of TE and TM. (b) The CD spectra are plotted based on the results derived from CMT, here θ_{TE} and θ_{TM} are acquired from the azimuthal angle of TE/TM eigenmodes in panel (a). (c), (e), (g) The amplitude and phase of the z component of the magnetic field for TE eigenmode for $\eta = 8.8°$, $24.8°$, and $31.3°$, respectively. (d), (f), (h) The amplitude and phase of the z component of the electric field for TM eigenmode for $\eta = 8.8°$, $24.8°$, and $31.3°$, respectively. The electromagnetic fields are extracted from $z = t/2$. The black arrows in panels (c)–(h) correspond to the electric field.

with the variation of the orientation angle and wavelength calculated by the modified CMT are shown in Fig. 4(b). The results based on the modified CMT are consistent with the simulation results in Fig. 2(d), which proves that the effective current orientation angles in the modified CMT are equal to the azimuthal angles of the corresponding polarization states. The other reflection spectra acquired from CMT are shown in Fig. S8 in the Supplemental Material [32].

To further clarify the statement above, we will illustrate the effective current orientation from a near-field electromagnetic diagram. For $\eta = 8.8°$, the amplitude and the phase of the z component of the magnetic field for TE$_1$ eigenmode are shown in Fig. 4(c), the black arrows denote the electric field, while the amplitude and the phase of the z component of electric field for TM$_2$ eigenmode are shown in Fig. 4(d). The near-field electric currents marked by white arrows are parallel with each other, which is consistent with the results of the overlapped azimuthal angles in Fig. 4(a). The phase patterns of the TE/TM eigenmodes are indicative of the in-plane wave vector's direction. As depicted in Figs. 4(c)–4(d), the phase trends for both eigenmodes align, signifying that their in-plane propagation directions are identical. This

correlation between phase patterns and propagation direction offers insights into the behavior and interaction of these eigenmodes within the photonic structure. For $\eta = 24.8°$, the angular difference of the near-field currents for TE$_2$ and TM$_2$ eigenmodes is nearly 135° as shown in Figs. 4(e) and 4(f), which matches well with the results of the corresponding azimuthal angles in Fig. 4(a) and contributes to the giant CD based on the modified CMT in Fig. 4(b). For $\eta = 31.3°$, the angular difference of the near-field currents for TE$_1$ and TM$_1$ eigenmodes are nearly orthogonal as shown in Figs. 4(g) and 4(h), which are in excellent agreement with the results of the azimuthal angles in Fig. 4(a). The phase patterns also show the relationship between the two modes. Thus, the degeneracy of TE$_1$ and TM$_1$ eigenmodes results in a weak chiroptical response as shown in Fig. 4(b). Furthermore, the optical near-field chirality, known as optical chirality (OC) density [38], is also provided in Fig. S9 in the Supplemental Material [32] (see also references [38,39] therein) to investigate the relationship between near-field OC and far-field CD. The results indicate a direct spectral correspondence between the difference in OC under RCP/LCP and CD at the three degeneracy points. This correspondence is consistent with the
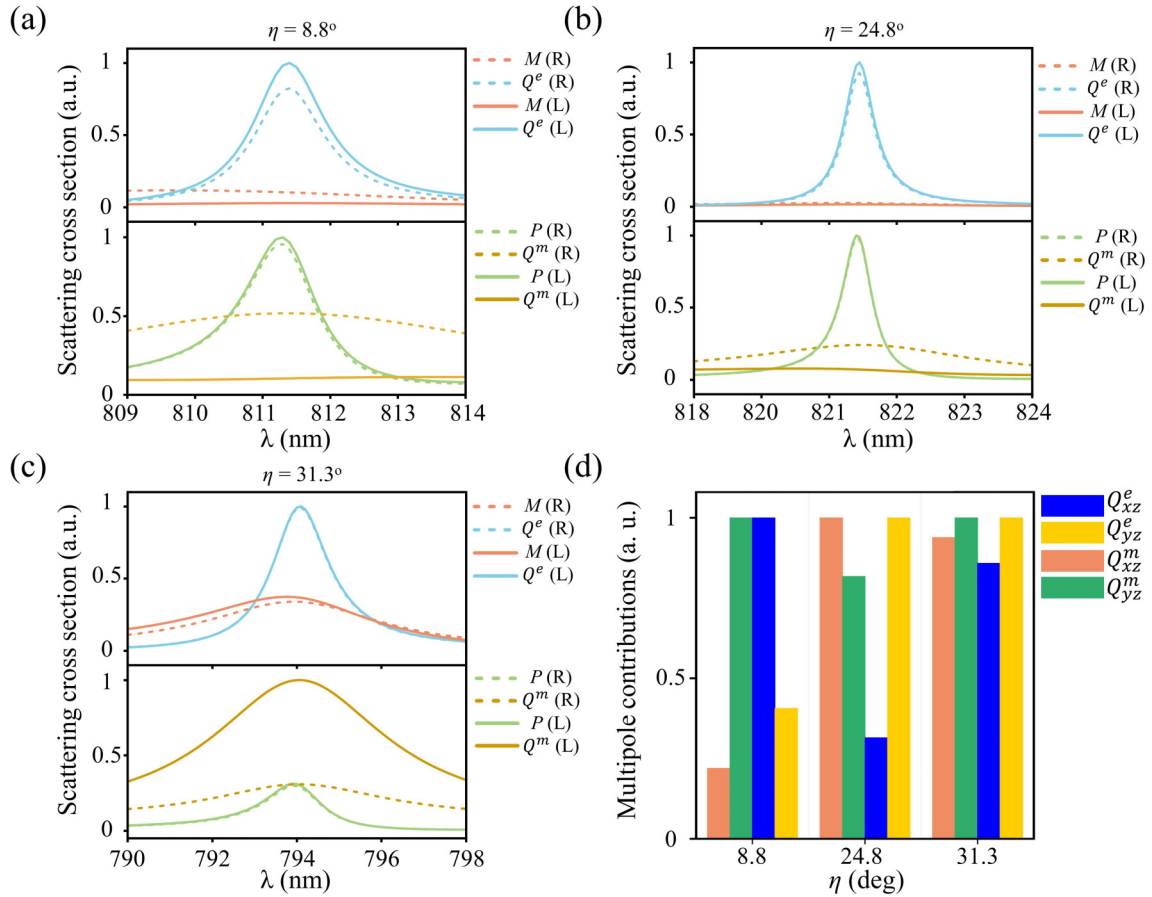
FIG. 5. Scattering cross-section spectra of electric dipole (P), magnetic dipole (M), electric quadrupole (Q^e), and magnetic quadrupole (Q^m) under RCP/LCP incidence for (a) $\eta = 8.8°$, (b) 24.8°, and (c) 31.3°, respectively. (d) Multipole contributions of the at-Γ TE/TM eigenmodes for $\eta = 8.8°$, 24.8°, and 31.3°, respectively, here xz and yz components of EQ and MQ are supported by TM and TE eigenmode individually.

results previously discovered in chiral metamaterial [39,40].

To more closely study the physical origin of this intrinsic chiral response at the three degeneracy points in Fig. 2(d), we studied the impact of multipole interactions. We calculate the scattering cross sections for electric dipole (P), magnetic dipole (M), electric quadrupole (Q^e), and magnetic quadrupole (Q^m) under RCP/LCP illumination, and the calculation methods are shown in Sec. 5 in the Supplemental Material [32] (see also Refs. [41,42] therein). To begin with, we analyze the multipole contributions for each TE and TM eigenmode with the variation of orientation angle in Fig. S10 in the Supplemental Material [32], from which we can see that M and Q^e are dominantly supported by TM eigenmode and P and Q^m are dominantly supported by TE eigenmode, thus the two pairs of electromagnetic multipoles are normalized, respectively, in Figs. 5(a)–5(c) to analyze the intrinsic chiroptical response supported by two individual eigenmodes. Here the multipole moments under RCP excitation are plotted by dashed lines and solid lines are used for that under LCP excitation. As shown in Fig. 5(a), for $\eta = 8.8°$, the main contributions are P, Q^e, and Q^m at the degenerate resonance wavelength. This phenomenon can be confirmed by electromagnetic field patterns. As shown in Figs. 4(c)–4(h), the amplitude of H_z and E_z of TE$_1$ and TM$_1$ eigenmode show two pairs of nodes, indicating the quadrupole-dominated response. For $\eta = 24.8°$, the dominant multipole contributions are P,

Q^e, and Q^m as shown in Fig. 5(b). The strength of Q^m displays differences for LCP and RCP incidence, which will contribute to the intrinsic chiroptical response. In Fig. 5(c), P, M, Q^e and Q^m all show a peak at the degenerate resonance wavelength for $\eta = 31.3°$. Note that in Figs. 5(a)–5(c), the Q^e is always dominant for TM mode at the three orientation angles. While for the multipole moments supported by TE mode, the P and Q^m strength is different for the three orientation angles. However, the obvious distinctions can be observed for the Q^m under LCP and RCP, which shows the irreplaceable role of Q^m for the intrinsic chirality. Thus, in the following, the multipole expansion for Q^e and Q^m under Cartesian coordinates is performed for the TE and TM eigenmodes in Fig. 5(d), and the xz and yz components of electric and magnetic quadrupole are dominated due to characteristics of TE (H_z-dominated) and TM (E_z-dominated) eigenmodes. The multipole contributions are normalized, respectively, at each orientation angle as shown in Fig. 5(d). For $\eta = 8.8°$, the intensity of Q^e_{xz} and Q^m_{yz} are larger than Q^e_{yz} and Q^m_{xz}, respectively, thus the nearly orthogonal electric and magnetic quadrupoles will cause the parallel effective current orientation of the corresponding TE and TM modes, which results in a small CD like that of the modified CMT. For $\eta = 31.3°$, we can see that the intensity of Q^e_{xz} and Q^m_{yz} are nearly the same as Q^e_{yz} and Q^m_{xz}, respectively, thus the nearly parallel electric and magnetic quadrupoles will cause the orthogonal effective current orientation, which also

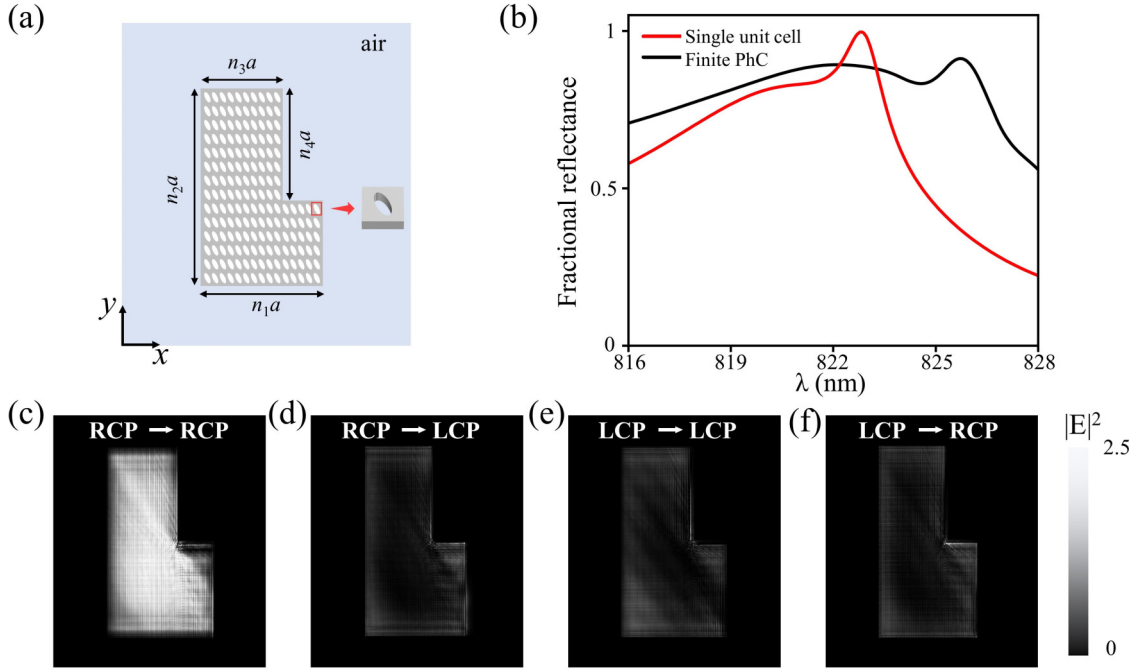FIG. 6. The spin-dependent reflection image based on the planar PhC. (a) Schematic of the pattern containing the letter L, n_1-n_4 are the numbers of the unit cells for this finite structure, and here $n_1 = 112$, $n_2 = 151$, $n_3 = 75$, $n_4 = 75$. (b) The fractional reflectivity (FR) spectra of the finite PhC structure as shown in Fig. 6(a) (black line) and the single unit cell with periodic boundary conditions (red line). (c) The RCP and (d) LCP component of the reflected electric field intensity under RCP illumination at $\lambda = 825.7$ nm. (e) The LCP and (f) RCP component of the reflected electric field intensity under LCP illumination at $\lambda = 825.7$ nm.

leads to near-zero CD. For $\eta = 24.8°$, the intensity of Q_{yz}^e is stronger than Q_{xz}^e, while the intensity of Q_{xz}^m and Q_{yz}^m are nearly equal, which causes the angle between the electric and magnetic quadrupoles to approach $45°/135°$, resulting in the giant CD like that of the modified CMT.

IV. SPIN-PRESERVING CHIRAL MIRROR FOR FINITE PHOTONIC CRYSTAL SLABS

The above study not only identified the largest intrinsic CD but also systematically investigated the physical mechanisms behind its formation. Notably, at an orientation angle $\eta = 24.8°$, RCP light is completely reflected while preserving its handedness, whereas the reflection of LCP light remains minimal. Importantly, this structural design is planar and does not necessitate any additional back-reflection mirrors. Thus, based on the designed spin-preserving PhC above, here we demonstrate the spin-dependent reflection image composed of an L shape as shown in Fig. 6(a). The L-shaped pattern contains elliptical air holes with orientation angle $\eta = 24.8°$, and the unit cell numbers of this finite structure composed of PhC are $n_1 = 112$, $n_2 = 151$, $n_3 = 75$, $n_4 = 75$. The fractional reflectivity spectra for the ideal single unit cell with periodical boundary conditions and finite PhC with perfect match layers are shown in Fig. 6(b). The fractional reflectivity (FR) is calculated as $\frac{R_{RR}}{(R_{RR}+R_{LR})}$, which reflects the proportion of spin-preserving reflection, for this finite structure, we can see that the FR approaches 1 at the resonant wavelength as shown in Fig. 6(b). To better compare the FR spectra acquired from a single unit cell of PhC and finite PhC

structure around the resonant wavelength, we also show the FR spectra of ideal infinite PhC as shown in Fig. 6(b). We can see that the FR results calculated from the finite PhC structure show a similar trend to that of the single unit cell. The slight deviation of resonant wavelength and the reduction in the amplitude of reflection are due to the finite geometrical structure. At resonant wavelength $\lambda_0 = 825.7$ nm, our results confirm the selective reflection of two different spin incident light with the FR approaching $\frac{R_{RR}}{(R_{RR}+R_{LR})} \approx 90\%$ and the extinction ratio up to $\frac{R_{RR}}{R_{LL}} = 9.3$ in the finite PhC structure. Such excellent spin-preserving strongly performs the previously reported structure, for example, Kang *et al.* reported spin mirrors with metallic substrate have an extinction ratio of $\sim$4 [14], Hu *et al.* designed asymmetric dimer-on-mirror metasurface showing an extinction ratio of $\sim$4.4 [43], and Gryb. et al proposed a rotated meta-atom with an extinction ratio of $\sim$7 [25]. To demonstrate the imaging performance of the PhC chiral mirrors, we display the reflection image of the different components under RCP and LCP incidence as shown in Figs. 6(c)–6(f). The RCP component of reflected electric field intensity under RCP illumination is significantly stronger than the other components. Thus, as a proof of concept, the proposed thin monolithic all-dielectric PhC with rotated elliptical air holes acts effectively as a spin-preserving mirror for image display.

V. CONCLUSIONS AND DISCUSSION

In conclusion, we propose a geometrically simple thin monolithic all-dielectric PhC with rotated elliptical air holes

to achieve a spin-preserving mirror by its intrinsically strong chiroptical response. This configuration introduces the orientation angle as a new degree of freedom to manipulate the chiroptical response. By adjusting the orientation angle, the TE and TM bands can be dynamically controlled, which causes the emergence of the degeneracy point of TE and TM modes. The maximum intrinsic CD appears at one degeneracy point, which can perfectly serve as a spin-preserving mirror. Combining the modified CMT and numerical simulation, we conclude that CD will be maximal when the angle difference between the effective currents of the TE and TM modes is 45 degrees, and when the in-plane currents of TE and TM modes are either orthogonal or parallel, CD will be zero. Moreover, the near-field patterns of TE and TM modes and multipole analysis are combined to further illustrate the relationship between the in-plane current orientation of TE and TM modes.

Finally, we demonstrate the potential applications of the imaging application composed of the designed PhC. This work not only opens perspectives in the novel design of spin-preserving mirrors, but also has potential applications for chiral quantum optics, and chiral light-matter interactions.

[1] E. Plum and N. I. Zheludev, Chiral mirrors, Appl. Phys. Lett. **106**, 221901 (2015).

[2] L. Jing, Z. Wang, R. Maturi, B. Zheng, H. Wang, Y. Yang, L. Shen, R. Hao, W. Yin, E. Li *et al.*, Gradient chiral metamirrors for spin-selective anomalous reflection, Laser Photon. Rev. **11**, 1700115 (2017).

[3] J. C. Zhang, M. K. Chen, Y. Liang, X. Hong, M. Wang, Y. Cheng, X. Liu, D. P. Tsai, and S. W. Pang, Nanoimprint meta-device for chiral imaging, Adv. Funct. Mater. **33**, 2306422 (2023).

[4] P. Lodahl, S. Mahmoodian, S. Stobbe, A. Rauschenbeutel, P. Schneeweiss, J. Volz, H. Pichler, and P. Zoller, Chiral quantum optics, Nature (London) **541**, 473 (2017).

[5] N. S. Baßler, A. Aiello, K. P. Schmidt, C. Genes, and M. Reitz, Metasurface-based hybrid optical cavities for chiral sensing, Phys. Rev. Lett. **132**, 043602 (2024).

[6] S.-M. Wang, Y.-F. Wang, L. Huang, L.-S. Zheng, H. Nian, Y.-T. Zheng, H. Yao, W. Jiang, X. Wang, and L.-P. Yang, Chiral recognition of neutral guests by chiral naphthotubes with a bisthiourea endo-functionalized cavity, Nat. Commun. **14**, 5645 (2023).

[7] T. Kan, A. Isozaki, N. Kanda, N. Nemoto, K. Konishi, H. Takahashi, M. Kuwata-Gonokami, K. Matsumoto, and I. Shimoyama, Enantiomeric switching of chiral metamaterial for terahertz polarization modulation employing vertically deformable MEMS spirals, Nat. Commun. **6**, 8422 (2015).

[8] Y. Zhao, M. Belkin, and A. Alù, Twisted optical metamaterials for planarized ultrathin broadband circular polarizers, Nat. Commun. **3**, 870 (2012).

[9] Z. Wang, Y. Wang, G. Adamo, B. H. Teh, Q. Y. S. Wu, J. Teng, and H. Sun, A novel chiral metasurface with controllable circular dichroism induced by coupling localized and propagating modes, Adv. Opt. Mater. **4**, 883 (2016).

[10] A. B. Khanikaev, N. Arju, Z. Fan, D. Purtseladze, F. Lu, J. Lee, P. Sarriugarte, M. Schnell, R. Hillenbrand, M. Belkin *et al.*, Experimental demonstration of the microscopic origin of circular dichroism in two-dimensional metamaterials, Nat. Commun. **7**, 12045 (2016).

[11] H. S. Khaliq, A. Nauman, J.-W. Lee, and H.-R. Kim, Recent progress on plasmonic and dielectric chiral metasurfaces:

Fundamentals, design strategies, and implementation, Adv. Opt. Mater. **11**, 2300644 (2023).

[12] Z. Ma, Y. Li, Y. Li, Y. Gong, S. A. Maier, and M. Hong, All-dielectric planar chiral metasurface with gradient geometric phase, Opt. Express **26**, 6067 (2018).

[13] A. Y. Zhu, W. T. Chen, A. Zaidi, Y.-W. Huang, M. Khorasaninejad, V. Sanjeev, C.-W. Qiu, and F. Capasso, Giant intrinsic chiro-optical activity in planar dielectric nanostructures, Light Sci. Appl. **7**, 17158 (2018).

[14] L. Kang, S. P. Rodrigues, M. Taghinejad, S. Lan, K.-T. Lee, Y. Liu, D. H. Werner, A. Urbas, and W. Cai, Preserving spin states upon reflection: Linear and nonlinear responses of a chiral meta-mirror, Nano Lett. **17**, 7102 (2017).

[15] Z. Li, W. Liu, H. Cheng, D.-Y. Choi, S. Chen, and J. Tian, Spin-selective full-dimensional manipulation of optical waves with chiral mirror, Adv. Mater. **32**, 1907983 (2020).

[16] W. Wu, Y. Battie, C. Genet, T. W. Ebbesen, G. Decher, and M. Pauly, Bottom-up tunable broadband semi-reflective chiral mirrors, Adv. Opt. Mater. **11**, 2202831 (2023).

[17] X. Xie, M. Pu, J. Jin, M. Xu, Y. Guo, X. Li, P. Gao, X. Ma, and X. Luo, Generalized Pancharatnam-Berry phase in rotationally symmetric meta-atoms, Phys. Rev. Lett. **126**, 183902 (2021).

[18] E. Karimi, S. A. Schulz, I. De Leon, H. Qassim, J. Upham, and R. W. Boyd, Generating optical orbital angular momentum at visible wavelengths using a plasmonic metasurface, Light Sci. Appl. **3**, e167 (2014).

[19] Q. Yang, M. Liu, S. Kruk, Y. Xu, Y. K. Srivastava, R. Singh, J. Han, Y. Kivshar, and I. V. Shadrivov, Polarization-sensitive dielectric membrane metasurfaces, Adv. Opt. Mater. **8**, 2000555 (2020).

[20] R. Gad, W. T. Lau, C. Nicholaou, S. Ahmadi, I. Sigal, and O. Levi, Tailoring of spectral response and spatial field distribution with corrugated photonic crystal slab, Opt. Lett. **40**, 3715 (2015).

[21] Z. Li, Y. Jiang, W. Liu, Y. Zhang, H. Cheng, J. Li, J. Tian, and S. Chen, Hybrid bilayer plasmonic metasurfaces with intrinsic chiral optical responses, Appl. Phys. Lett. **122**, 181702 (2023).

[22] J. Meng, Z. Zhang, W. Liu, Y. Li, Y. Sun, Z. Lai, and T. Yu, Angle-selective chiral absorption induced by diffractive coupling in metasurfaces, Opt. Lett. **47**, 5385 (2022).

[23] Y. Zeng, Q. Duan, J. Xu, Z. Yang, H. Chen, and Y. Liu, Tunable circular conversion dichroism of single-layer twisted graphene-patterned metasurface, iScience **26**, 106115 (2023).

[24] T. Cao, C. Wei, and L. Zhang, Modeling of multi-band circular dichroism using metal/dielectric/metal achiral metamaterials, Opt. Mater. Express **4**, 1526 (2014).

[25] D. Gryb, F. J. Wendisch, A. Aigner, T. Gölz, A. Tittl, L. de S. Menezes, and S. A. Maier, Two-dimensional chiral meta-surfaces obtained by geometrically simple meta-atom rotations, Nano Lett. **23**, 8891 (2023).

[26] H. Ali, E. Petronijevic, G. Pellegrini, C. Sibilia, and L. C. Andreani, Circular dichroism in a plasmonic array of elliptical nanoholes with square lattice, Opt. Express **31**, 14196 (2023).

[27] N. Apurv Chaitanya, M. Butt, O. Reshef, R. W. Boyd, P. Banzer, and I. De Leon, Lattice-plasmon-induced asymmetric transmission in two-dimensional chiral arrays, APL Photon. **7**, 016105 (2022).

[28] B. Semnani, J. Flannery, R. Al Maruf, and M. Bajcsy, Spin-preserving chiral photonic crystal mirror, Light Sci. Appl. **9**, 23 (2020).

[29] K. Voronin, A. S. Taradin, M. V. Gorkunov, and D. G. Baranov, Single-handedness chiral optical cavities, ACS Photon. **9**, 2652 (2022).

[30] W. Ye, Y. Gao, and J. Liu, Singular points of polarizations in the momentum space of photonic crystal slabs, Phys. Rev. Lett. **124**, 153904 (2020).

[31] Q. Duan, Y. Zeng, Y. Yin, J. Xu, Z. Chen, Z. Hao, H. Chen, and Y. Liu, Photonic crystal slabs with maximal chiroptical response empowered by bound states in the continuum, Photon. Res. **11**, 1919 (2023).

[32] See Supplemental Material at http://link.aps.org/supplemental/10.1103/PhysRevB.110.115401 for details, TCMT for a single TE/TM eigenstate, TCMT for the degeneration of TE and TM eigenstates, TCMT for two pairs of TE and TM eigenstates, the scattering cross sections of multipole moments under Cartesian coordinate, and which includes Refs. [29,33–35,38,39,41,42].

[33] S. Fan, W. Suh, and J. D. Joannopoulos, Temporal coupled-mode theory for the Fano resonance in optical resonators, J. Opt. Soc. Am. A **20**, 569 (2003).

[34] W. Suh, Z. Wang, and S. Fan, Temporal coupled-mode theory and the presence of non-orthogonal modes in lossless multi-mode cavities, IEEE J. Quantum Electron. **40**, 1511 (2004).

[35] N. Parappurath, F. Alpeggiani, L. Kuipers, and E. Verhagen, The origin and limit of asymmetric transmission in chiral resonators, ACS Photon. **4**, 884 (2017).

[36] S. Fan and J. D. Joannopoulos, Analysis of guided resonances in photonic crystal slabs, Phys. Rev. B **65**, 235112 (2002).

[37] T. Shi, Z.-L. Deng, G. Geng, X. Zeng, Y. Zeng, G. Hu, A. Overvig, J. Li, C.-W. Qiu, A. Alù *et al.*, Planar chiral metasurfaces with maximal and tunable chiroptical response driven by bound states in the continuum, Nat. Commun. **13**, 4111 (2022).

[38] Y. Tang and A. E. Cohen, Optical chirality and its interaction with matter, Phys. Rev. Lett. **104**, 163901 (2010).

[39] G. Long, G. Adamo, J. Tian, M. Klein, H. N. Krishnamoorthy, E. Feltri, H. Wang, and C. Soci, Perovskite metasurfaces with large superstructural chirality, Nat. Commun. **13**, 1551 (2022).

[40] S. Zanotto, G. Mazzamuto, F. Riboli, G. Biasiol, G. C. La Rocca, A. Tredicucci, and A. Pitanti, Photonic bands, super-chirality, and inverse design of a chiral minimal metasurface, Nanophotonics **8**, 2291 (2019).

[41] A. B. Evlyukhin and B. N. Chichkov, Multipole decompositions for directional light scattering, Phys. Rev. B **100**, 125415 (2019).

[42] P. D. Terekhov, A. B. Evlyukhin, D. Redka, V. S. Volkov, A. S. Shalin, and A. Karabchevsky, Magnetic octupole response of dielectric quadrumers, Laser Photon. Rev. **14**, 1900331 (2020).

[43] J. Hu, Y. Xiao, L.-M. Zhou, X. Jiang, W. Qiu, W. Fei, Y. Chen, and Q. Zhan, Ultra-narrow-band circular dichroism by surface lattice resonances in an asymmetric dimer-on-mirror metasurface, Opt. Express **30**, 16020 (2022).